


AUGUST 25 2023

Physics-based scintillations for outdoor sound auralization



Andrea P. C. Bresciani ; Julien Maillard; Leandro D. de Santana



J. Acoust. Soc. Am. 154, 1179–1190 (2023)

<https://doi.org/10.1121/10.0020666>



View
Online



Export
Citation

CrossMark

Articles You May Be Interested In

Auralization of aircraft flyovers with turbulence-induced coherence loss in ground effect

J. Acoust. Soc. Am. (April 2022)

Auralization of municipal public address announcements by applying geometrical sound simulation and multi-channel reproduction techniques

Proc. Mtgs. Acoust. (June 2013)

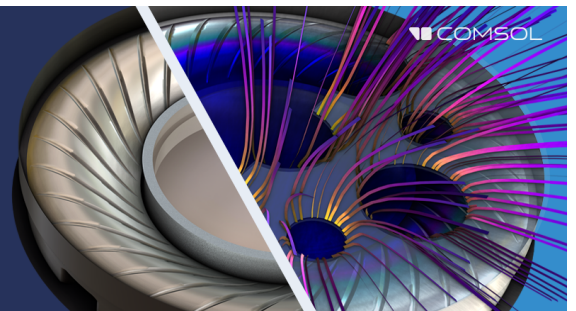
Auralization of municipal public address announcements by applying geometrical sound simulation and multi-channel reproduction techniques

J Acoust Soc Am (May 2013)

Take the Lead in Acoustics

The ability to account for coupled physics phenomena lets you predict, optimize, and virtually test a design under real-world conditions – even before a first prototype is built.

» Learn more about COMSOL Multiphysics®



Physics-based scintillations for outdoor sound auralization

Andrea P. C. Bresciani,^{1,a)}  Julien Maillard,² and Leandro D. de Santana¹

¹University of Twente, P.O. Box 217, Enschede, 7500 AE, the Netherlands

²Centre Scientifique et Technique du Bâtiment (CSTB), Saint-Martin-d'Hères, 38400, France

ABSTRACT:

The sound propagating in a turbulent atmosphere fluctuates in amplitude and phase. This phenomenon, known as acoustic scintillation, is caused by random fluctuations in the acoustic refractive index of the air induced by atmospheric turbulence. Auralization techniques should consider this phenomenon to increase the realism of the synthetic sound. This paper proposes a physics-based formulation to model sequences of log-amplitude and phase fluctuations of a sound propagating in a turbulent atmosphere. This method applies to slanted and vertical propagation of the sound, which is useful for simulating elevated noise sources such as aircraft, drones, and wind turbines. The theoretical framework is based on the spatial correlation functions for the log-amplitude and phase fluctuations for spherical waves, the von Kármán spectrum, and similarity theories to model atmospheric turbulence. Two applications with audio files are presented to demonstrate the applicability of this method to tonal and broadband noise.

© 2023 Acoustical Society of America. <https://doi.org/10.1121/10.0020666>

(Received 25 April 2023; revised 19 July 2023; accepted 29 July 2023; published online 25 August 2023)

[Editor: Vladimir E Ostashev]

Pages: 1179–1190

I. INTRODUCTION

A sound wave propagating in a turbulent medium encounters variations in the acoustic refractive index caused by random fluctuations in temperature and velocity. As a result, the wave is randomly distorted, causing changes in its amplitude and phase. For example, for a pure tone emitted by a static source, a listener sufficiently far away will perceive a fluctuation (around the nominal, undisturbed values) in amplitude and frequency. An example is provided in Mm. 4 as an audio file, and it will be presented in detail in Sec. VI. While the variation in the perceived amplitude is directly related to the variation in amplitude of the acoustic wave, the perceived fluctuation of the sound frequency is due to the time-varying phase of the wave reaching the listener. The fluctuation of the phase and amplitude of an acoustic wave in a turbulent medium is known as acoustic scintillation. This phenomenon is also observed in electromagnetic waves being applied to optics and influencing astronomical observations. In the field of acoustics, the research on scintillation focuses mainly on sound propagating in the ocean and atmosphere. This paper deals with atmospheric sound propagation.

Auralization techniques for sound propagating in the atmosphere should include acoustic scintillation to improve realism. A few models have been proposed in previous literature to describe the amplitude and phase fluctuations. [Pieren *et al.* \(2014\)](#) used an empirical model based on low-pass filtered white noise to predict the stochastic amplitude fluctuation of wind turbine noise. The authors chose the

cutoff frequency of the low-pass filter by fitting 20 measurements. In this work, the fluctuation in phase was neglected. An attempt to use a model based on a Gaussian turbulence spectrum to describe the log-amplitude and phase fluctuations of wind turbine noise was reported by [Heutschi *et al.* \(2014\)](#). The model is described by [Daigle *et al.* \(1983\)](#) and recalled in Sec. II. However, [Daigle *et al.* \(1983\)](#) noticed that the predicted log-amplitude fluctuations are higher than the measured values. Furthermore, the model relies on a turbulence length scale for the fluctuation of the refractive index, which makes it difficult to estimate for slanted propagation paths as it varies with height. The same model was used by [Rietdijk *et al.* \(2017\)](#), who focused on developing a methodology to generate sequences of acoustic scintillations based on the correlation functions of the phase and log-amplitude fluctuations. [Rietdijk *et al.* \(2017\)](#) applied this methodology to aircraft noise synthesis. More recently, [Pieren and Lincke \(2022\)](#) proposed to apply the same theoretical framework used in the present work to model the loss of coherence between the direct and the ground-reflected path. Similarly, [Lincke *et al.* \(2023\)](#) applied the same methodology to model the loss of coherence between microphones. This approach indirectly accounts for phase fluctuations.

In the present work, we further develop the methodology of [Rietdijk *et al.* \(2017\)](#) to generate acoustic scintillations by calculating the correlation functions for the log-amplitude and phase fluctuations with a more rigorous physical model. We exploit the analytical solution of the narrow-angle parabolic equation for a sound propagating in a turbulent media as calculated by [Ostashev and Wilson \(2016\)](#). The analytical solution is obtained using the Markov approximation and Rytov method. The von Kármán spectrum, mixed-layer, and Monin–Obukhov similarity theories

^{a)}Also at: Centre Scientifique et Technique du Bâtiment (CSTB), Saint-Martin-d'Hères, 38400, France. Email: a.p.c.bresciani@utwente.nl

are used to model the height-dependent temperature and velocity fluctuations, extending the applicability of previous methodologies to vertical and slanted propagation paths. Compared to the methods used in previous literature (Heutschi *et al.*, 2014; Rietdijk *et al.*, 2017), the proposed approach overcomes the difficulty of choosing the proper turbulence length scale, as it is now modeled by the similarity theories.

The theory presented in this paper has been developed for line-of-sight propagation, i.e., the effect of atmospheric refraction on the propagation path is supposed negligible. Furthermore, a single, straight propagation path between the source and receiver is assumed. In practice, this happens for ground-based receivers and elevated noise sources, such as airplanes, helicopters, and wind turbines, or vice versa for ground-based sources and elevated receivers.

The paper is organized as follows. Section II recalls the Gaussian model of Daigle *et al.* (1983), highlighting its limitations. Section III describes the proposed approach based on the correlation functions for spherical wave propagation, the Monin–Obukhov and mixed-layer similarity theories, and the von Kármán spectrum and compares the correlation functions with the previous model. Section IV presents a simple method used to account for the saturation of the log-amplitude fluctuations. Section V recalls the methodology to obtain the time series of the log-amplitude and phase fluctuations and presents results for several atmospheric conditions and source-receiver configurations. Section VI presents two possible applications with the support of audio files, highlighting critical points and suggesting possible future works. Finally, Sec. VII summarizes the results.

II. GAUSSIAN MODEL FOR THE REFRACTIVE INDEX FLUCTUATIONS

Daigle *et al.* (1983) experimentally analyzed the horizontal propagation near the ground and compared the variances of the log-amplitude and phase fluctuations with the prediction obtained with a simple theory. The theory is based on the Gaussian model of the two-point correlation function, B_μ , of the acoustic refractive index fluctuations, μ ,

$$B_\mu(\zeta) = \sigma_\mu^2 \exp(-\zeta^2/\mathcal{L}^2), \quad (1)$$

where ζ represents the separation distance, σ_μ^2 denotes the variance of the refractive index fluctuations, and \mathcal{L} is a measure of the scale of turbulence. The acoustic refractive index is defined as $\mu_0 = c_0/(c + \mathbf{n} \cdot \tilde{\mathbf{v}})$ (Ostashev and Wilson, 2016), where c and c_0 represent the speed of sound and its mean value, respectively, \mathbf{n} is the unit vector normal to the wavefront, and $\tilde{\mathbf{v}}$ denotes the velocity fluctuations of the medium. Neglecting the second-order terms and supposing $\mathbf{n} = (1, 0, 0)$, the fluctuation of the refractive index is $\mu = -(\tilde{c} + \tilde{v}_x)/c_0$, where $\tilde{c} = c - c_0$ is the fluctuating part of the speed of sound, and \tilde{v}_x is the x component of the medium velocity fluctuations. For $\mathcal{L} \ll \sqrt{\lambda L}$, i.e., assuming the Markov approximation (Daigle *et al.*, 1983), where λ is the acoustic wavelength, L is the propagation distance, the

variance of the log-amplitude and phase fluctuations, σ_χ^2 and σ_ϕ^2 , respectively, can be written for spherical waves with the Rytov method as (Daigle *et al.*, 1983)

$$\sigma_\chi^2 = \sigma_\phi^2 = \frac{\sqrt{\pi}}{2} \sigma_\mu^2 k^2 L \mathcal{L}, \quad (2)$$

where $k = \omega/c_0$ is the acoustic wavenumber. The correlation functions for the log-amplitude and phase fluctuations, $B_\chi(\zeta)$ and $B_\phi(\zeta)$, are expressed as

$$\frac{B_\chi(\zeta)}{\sigma_\chi^2} = \frac{B_\phi(\zeta)}{\sigma_\phi^2} = \frac{\Phi(\zeta/\mathcal{L})}{\zeta/\mathcal{L}}, \quad (3)$$

where

$$\Phi(\zeta/\mathcal{L}) = \int_0^{\zeta/\mathcal{L}} \exp(-u^2) du = \frac{\sqrt{\pi}}{2} \text{erf}(\zeta/\mathcal{L}), \quad (4)$$

and $\text{erf}(x)$ is the error function. The prefix *log* in *log-amplitude* is commonly used in the literature to remind the reader that the amplitude of the distorted wave, A , is related to the log-amplitude, χ , through the relation $\chi = \ln(A/A_0)$, where A_0 is the amplitude of the undistorted wave. This relation is a direct consequence of the Rytov method.

Daigle *et al.* (1978) inferred the turbulence length scale, \mathcal{L} , by fitting Eq. (1) with the measured autocorrelation function. They found values ranging between 1 and 1.5 m for horizontal propagation between 0.15 and 5 m above the ground. In Daigle *et al.* (1983), $\mathcal{L} = 1.1$ m was used to compare the numerical predictions with the measurements. A good agreement was found for the phase variance. The log-amplitude variance, however, was overestimated by the theory. Although a choice for \mathcal{L} is possible for horizontal propagation, it is difficult to define a univocal value for slanted or vertical propagation as the value of \mathcal{L} is strongly affected by height.

Another point to be addressed is the choice of the value for the refractive index variance, σ_μ^2 . It is calculated from the variances of the velocity and temperature fluctuations, σ_v^2 and σ_T^2 , using the approximation (e.g., Daigle *et al.*, 1983)

$$\sigma_\mu^2 \approx \frac{\sigma_v^2}{c_0^2} + \frac{\sigma_T^2}{4T_0^2}, \quad (5)$$

where T_0 is the mean temperature. Experiments of Daigle *et al.* (1983) suggested values for σ_μ^2 ranging from 10^{-6} to 10^{-5} depending on the atmospheric conditions. For horizontal propagation, the choice of σ_μ^2 is possible and can even be modeled using similarity theories. However, its value is expected to change with the height above ground. Thus, the limitation highlighted for the turbulence scale, \mathcal{L} , holds also for σ_μ^2 . That is, it is difficult to choose a single value for σ_μ^2 in the case of slanted or vertical propagation.

The Gaussian model described by Daigle *et al.* (1983) and recalled in this section differs from the revised and more accurate model described by Ostashev and Wilson

(2016) in Sec. 7.3.1.3. First, [Ostashev and Wilson \(2016\)](#) consider the velocity fluctuations of a random *vector* field, which implies that Eqs. (1) and (5) are replaced by the correct Gaussian turbulence spectrum [Eq. (7.36) of [Ostashev and Wilson, 2016](#)]. As a result, the term corresponding to the velocity fluctuations depends on the turbulence wavenumber squared, κ^2 . This dependency is not obtained with the simplified model described in this section. Second, the variances and correlation functions of the phase and log-amplitude fluctuations are calculated more accurately, thus, replacing Eqs. (2) and (3) with Eqs. (7.113) and (7.114), for plane wave propagation. Finally, Secs. 6.2.3 and 6.2.4 in [Ostashev and Wilson \(2016\)](#) enable calculating the variances and length scales of temperature and velocity fluctuations for the Gaussian model in terms of the meteorological parameters.

Section III explains a theoretical framework that allows calculating the correlation functions for a height-dependent turbulence spectrum. Therefore, in this framework, the mixed-layer and Monin–Obukhov similarity theories can be used to model the variance and length scale of the temperature and velocity fluctuations.

III. CORRELATION FUNCTIONS FOR PHASE AND LOG-AMPLITUDE FLUCTUATIONS

A. Theory

The correlation function of the phase and log-amplitude fluctuations for a ground-based source and elevated receiver, as shown in Fig. 1(a), is given by [Ostashev and Wilson \(2018\)](#), Eq. (77), as

$$B_{\phi,z}(L, \zeta) = \frac{\pi^2 k^2}{2} \int_0^L dl \int_0^\infty \Phi_{\text{eff}}(l \cos \theta, \kappa) J_0(l\kappa\zeta/L) \times \left[1 \pm \cos \left(\frac{l}{L} \left(1 - \frac{l}{L} \right) \frac{\kappa^2 L}{k} \right) \right] \kappa d\kappa. \quad (6)$$

In Eq. (6), the “+” and “−” signs apply to B_ϕ and B_z , respectively; l represents the coordinate from source to receiver; $\Phi_{\text{eff}}(z, \kappa)$ is the effective turbulence spectrum of the acoustic refractive index as a function of height above ground, z , and turbulence wavenumber, κ ; θ denotes the angle between the vertical direction and the propagation direction; and J_0 is the Bessel function of the first kind and zero order. Equation (6)

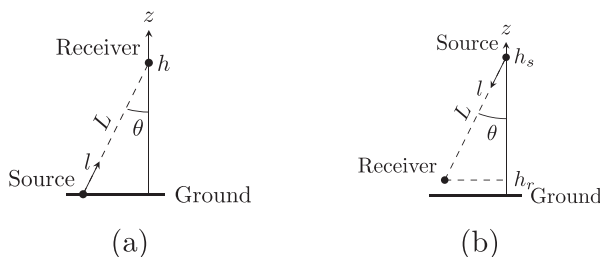


FIG. 1. Reference frames for slanted propagation, showing (a) ground-based source and (b) elevated source.

is a two-dimensional integral along the propagation path and turbulence wavenumber. It requires specifying the effective turbulence spectrum, which varies along the path in the case of non-horizontal propagation.

Equation (6) is derived for spherical waves using the Markov approximation and Rytov method. For brevity, the Rytov method is not discussed here as details can be found in Sec. 7 of [Ostashev and Wilson \(2016\)](#). The Markov approximation is expected to be valid if the propagation length is much larger than the length scale of the inhomogeneities affecting the corresponding statistical moment ([Ostashev et al., 2022; Ostashev and Wilson, 2019](#)), which significantly simplifies their calculation. Recently, [Ostashev et al. \(2022\)](#) derived the expression for the phase variance, $\sigma_\phi^2(L) = B_\phi(L, \zeta = 0)$, without using the Markov approximation. Although it can probably be generalized for any value of ζ , this new formulation also agrees better with experimental data, whereas the variance computed with the Markov approximation overpredicts the measurements. For long propagation distances, the difference between the two formulations tends toward a constant value. The main focus of this work is the auralization of broadband noise, for which we expect the phase fluctuations to be difficult to perceive. For this reason, the new formulation proposed by [Ostashev et al. \(2022\)](#) is not used in the present work. However, it should be considered when auralizing tonal noises for which the phase changes are clearly audible.

We rewrite Eq. (6), introducing the source and receiver heights, h_s and h_r , respectively. A schematic representation of the problem is depicted in Fig. 1(b). We repeat that Eq. (6) was derived supposing a single, straight propagation path between source and receiver. This hypothesis is implicitly satisfied if either source or receiver is at ground level. The configuration depicted in Fig. 1(b), where $h_r > 0$ and $h_s > 0$ violates this assumption, and the formulation is then strictly valid for the direct path only. However, as a first approximation, we assume that for situations where the height of the source is significantly larger than the height of the receiver (or vice versa), the phase and log-amplitude modulation of the ground-reflected path is equivalent to that of the direct path. As shown in previous publications ([Arntzen and Simons, 2014; Lincke et al., 2023; Pieren and Lincke, 2022; Rizzi and Sahai, 2019](#)), this approximation in the case of the phase fluctuations is only true at low frequencies.

Following [Ostashev and Wilson \(2018\)](#), the integration has to be performed from the source ($l=0$), which is now at $z=h_s$, to the receiver ($l=L$) at $z=h_r$ (in [Ostashev and Wilson, 2018](#), $h_r=0$). If we define $\eta = l/L$, Eq. (6) becomes

$$B_{\phi,z}(L, \zeta) = \frac{\pi^2 k^2 L}{2} \int_0^1 d\eta \int_0^\infty \Phi_{\text{eff}}((1-\eta)h_s + \eta h_r, \kappa) \times J_0(\eta\kappa\zeta) \left[1 \pm \cos \left(\frac{\eta(1-\eta)\kappa^2 L}{k} \right) \right] \kappa d\kappa, \quad (7)$$

where Φ_{eff} is now correctly evaluated at h_s when $\eta = 0$ (i.e., the source position) and h_r when $\eta = 1$ (i.e., the receiver position).

We now introduce the von Kármán effective turbulence spectrum for the refractive index fluctuations (see, e.g., Kamrath *et al.*, 2021) as

$$\Phi_{\text{eff}}(z, \kappa) = \frac{\Gamma(11/6)}{\pi^{3/2}\Gamma(1/3)} \left[\frac{\sigma_T^2(z)L_T^3(z)}{T_0^2(1 + \kappa^2L_T^2(z))^{11/6}} + \frac{22}{3} \frac{\sigma_{v,s}^2L_{v,s}^5(z)\kappa^2}{c_0^2(1 + \kappa^2L_{v,s}^2(z))^{17/6}} + \frac{22}{3} \frac{\sigma_{v,b}^2L_{v,b}^5(z)\kappa^2}{c_0^2(1 + \kappa^2L_{v,b}^2(z))^{17/6}} \right]. \quad (8)$$

The first term in the square brackets models the temperature fluctuations, where σ_T^2 denotes the variance and L_T represents the length scale. The second and third terms are associated with velocity fluctuations due to shear, subscript (v,s) , and buoyancy, subscript (v,b) , respectively. The associated variances and length scales are denoted $\sigma_{v,s}^2$ and $\sigma_{v,b}^2$ and $L_{v,s}$ and $L_{v,b}$, respectively. Substituting Eq. (8) into Eq. (7) results in integrals that cannot be evaluated analytically (Ostashev and Wilson, 2016).

Recently, Kamrath *et al.* (2021) applied the same model, i.e., Eq. (6) with the spectrum given in Eq. (8), to predict the variance for the log-amplitude and phase fluctuations. The authors compared the predictions with measurements. Although the log-amplitude variance agreed well with the model, the phase variance was overestimated. However, if the buoyancy effects were neglected, the predictions of the phase variance agreed well with the data. This has been explained by the limitation of the turbulence model, which is unable to capture the large-scale structures due to buoyancy-induced turbulence near the ground. This effect is called the *blocking effect*. As a turbulence model able to capture this effect has not been yet developed, we neglect the contribution of the buoyancy to the spectrum when we calculate the correlation function for the phase fluctuations, i.e., $\sigma_{v,b} = 0$ in Eq. (8).

It should be noted that the Gaussian effective turbulence spectrum given in Eq. (7.36) of Ostashev and Wilson (2016) could be used in place of Eq. (8). This assumes that the acoustic propagation in the atmosphere is mainly affected by large structures that are well modeled by the Gaussian spectrum. In this case, the computational cost is lower because the calculation of the correlation functions requires the computation of a one-dimensional integral in η , i.e., Eqs. (7.120) and (7.121) from Ostashev and Wilson (2016), instead of a two-dimensional integral as for the von Kármán spectrum. We choose to use the von Kármán spectrum as the reduction in computational cost is not substantial when considering the entire auralization process described in Sec. V. Furthermore, the von Kármán spectrum has been shown

to yield more accurate results in wind tunnel-scaled experiments compared to the Gaussian spectrum (Biesheuvel *et al.*, 2019). This is expected as, unlike the Gaussian model, the von Kármán spectrum is a physics-based spectrum because it coincides with the Kolmogorov spectrum in the inertial subrange of turbulence. Moreover, small-scale turbulence affects the log-amplitude fluctuations, hence, it can be argued that the Gaussian spectrum and Eq. (7.121) cannot be used to model the log-amplitude fluctuations. Finally, the application of Eq. (7.120) to the phase fluctuations is doubtful and should be verified.

Ostashev and Wilson (2016), in Secs. 2.2.3 and 6.2.4, presented the Monin–Obukhov similarity theory, which is useful to model the variance and length scale of temperature and shear-produced velocity fluctuations in the atmospheric surface layer. This theory applies to atmospheric conditions ranging from strongly unstable to slightly stable, and it cannot be used to model from moderately to strongly stable conditions. The buoyancy-produced velocity fluctuations are modeled with the mixed-layer similarity theory. The variances and length scales can be calculated from the surface heat flux, Q_H , friction velocity, u_* , and boundary layer height, z_i , as

$$\sigma_T^2(z) = \frac{4.0T_*^2}{(1 - 10z/L_o)^{2/3}}, \quad \sigma_{v,s}^2 = 3.0u_*^2, \quad \sigma_{v,b}^2 = 0.35w_*^2, \quad (9)$$

$$L_T(z) = 2.0z \frac{1 - 7z/L_o}{1 - 10z/L_o}, \quad L_{v,s}(z) = 1.8z, \quad L_{v,b} = 0.23z_i, \quad (10)$$

where $T_* = -Q_H/(\rho_0c_Pu_*)$ represents the surface layer temperature scale, $L_o = -u_*^3T_s\rho_0c_P/(g\kappa_vQ_H)$ denotes the Obukhov length, and $w_* = [z_i g Q_H / (\rho_0 c_P T_s)]^{1/3}$ is the velocity scale for the buoyancy-induced turbulence. In the definitions of T_* , L_o , and w_* , ρ_0 represents the reference density, c_P is the specific heat at constant pressure, T_s is the surface temperature, g represents the gravitational force per unit mass, and $\kappa_v = 0.4$ is the von Kármán constant. Values for the surface heat flux, Q_H , range from 200 W/m² for a sunny day, i.e., strongly unstable conditions, to -20 W/m² for clear skies at night and strong wind, i.e., strongly stable conditions (Ostashev and Wilson, 2016). For mostly cloudy conditions, values around 0 W/m², i.e., neutral atmosphere, can be chosen (Ostashev and Wilson, 2016). The friction velocity, u_* , depends on the wind speed and ranges from 0.05 m/s for zero or very light wind to 0.7 m/s for strong wind (Ostashev and Wilson, 2018). Finally, the boundary layer height, z_i , depends on the site and atmospheric conditions. A typical value during daytime and with a relatively flat terrain is 1000 m (Kamrath *et al.*, 2021; Ostashev and Wilson, 2016).

Figure 2 shows the block diagram that summarizes the calculation process for the correlation functions. First, the similarity theories are used to model the variance and length scale values [Eqs. (9) and (10)], which appear in the von Kármán spectrum [Eq. (8)]. Then, the von Kármán spectrum

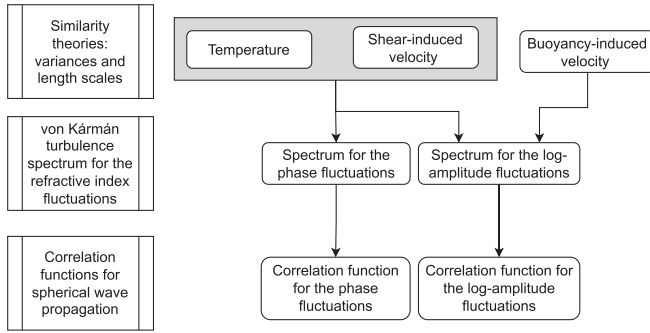


FIG. 2. Block diagram shows the calculation process for the phase and log-amplitude correlation functions. The gray box, including “temperature” and “shear-induced velocity,” indicate that both contributions are considered.

is used in Eq. (7) to calculate the correlation functions for the log-amplitude and phase fluctuations.

B. Comparison between von Kármán and Gaussian models

Figure 3 shows the correlation functions for the Gaussian model of Daigle et al. (1983), i.e., Eqs. (2)–(5), compared with the von Kármán model explained in this section. The variances of temperature and velocity are calculated for both models using the similarity theories described in this section. The comparison is shown for horizontal propagation near the ground (2 m height) as the correlation length $\mathcal{L} = 1.1$ m used for the Gaussian model is known from measurements (Daigle et al., 1983) and can be supposed to be constant along the propagation path. We highlight that the horizontal propagation close to the ground violates the single path assumption introduced above due to the presence of the ground-reflected path. Hence, Eq. (7) and the model described in Sec. II are not strictly applicable. However, the comparison remains meaningful as both models rely on that same assumption. Furthermore, as already mentioned, the comparison for elevated sources (or receivers) would be difficult as the correlation length changes along the propagation path.

The variance of the Gaussian model for the phase differs from the variance for the log-amplitude, despite Eq. (2), because σ_μ^2 for the phase variance is calculated by neglecting the buoyancy effect. This is consistent with the approach followed for the von Kármán model. Therefore, for the

phase variance, Eq. (5) is used with $\sigma_v^2 = \sigma_{v,s}^2$, whereas for the log-amplitude variance, $\sigma_v^2 = \sigma_{v,s}^2 + \sigma_{v,b}^2$. As a result, the Gaussian model overestimates the log-amplitude variance while it underestimates the phase variance compared to the von Kármán model. Furthermore, the shape of the correlation functions is not correctly reproduced by the Gaussian model, i.e., for the log-amplitude fluctuations, the decay of the Gaussian model is longer than that for the von Kármán model, whereas it is shorter for the phase fluctuations. As shown in Sec. V, this will affect the spectrum of the scintillation sequences. It is recalled that the log-amplitude variance predicted with the von Kármán model is closer to the measurements (Kamrath et al., 2021) than that calculated with the Gaussian model (Daigle et al., 1983).

In Fig. 3, we scaled the correlation function with the variance and the separation distance, ζ , with the radius of the first Fresnel zone, $\sqrt{\lambda L}$, where λ is the wavelength. With this scaling, B_ζ reaches negligible values with increasing ζ independently on the source height, frequency, atmospheric conditions (Q_H and u_*), and distance. With the same scaling, the shape of the correlation function for the phase is independent of the atmospheric conditions (Q_H and u_*), but it still depends on the source height, frequency, and distance. From a practical point of view, the scaling properties are useful to automatically calculate a maximum value of ζ above which the correlation functions are approximately zero. These properties will be applied in Sec. V. Furthermore, the scaling observed for the log-amplitude correlation can be exploited to reduce the computational cost by, e.g., calculating the function for a single frequency and applying the scaling factor to obtain the function at the remaining frequencies.

The log-amplitude correlation function reaches negligible values for $\zeta \approx 2\sqrt{\lambda L}$, whereas the decay of the phase correlation function is approximately ten times longer. As large values of ζ correspond to large turbulence structures, the phase fluctuations are induced by larger turbulent eddies compared to those that induce the log-amplitude fluctuations (Kamrath et al., 2021).

IV. SATURATION OF THE LOG-AMPLITUDE FLUCTUATIONS

The models for the correlation functions of the log-amplitude fluctuations given in Eqs. (3) and (7) are expected

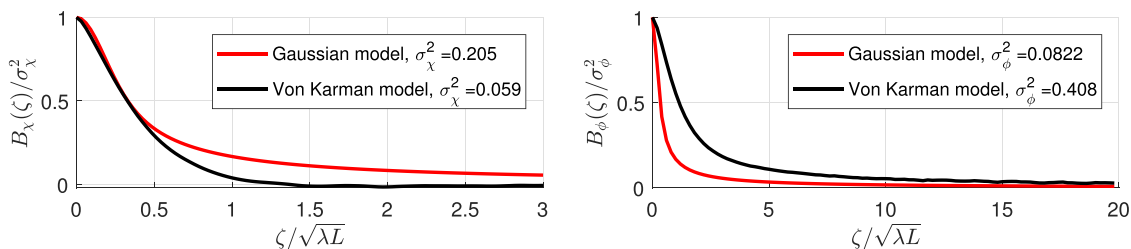


FIG. 3. (Color online) Correlation functions for the (left) log-amplitude, B_ζ , and (right) phase fluctuations, B_ϕ , normalized by the respective variances. The sensor separation, ζ , is normalized by the radius of the first Fresnel zone, $\sqrt{\lambda L}$. The correlation functions are calculated for a source-receiver distance, $L = 100$ m, and horizontal propagation with $h_s = h_r = 2$ m. The frequency is 1 kHz. The atmospheric surface layer is modeled using similarity theories with $Q_H = 50$ W/m², $u_* = 0.3$ m/s, and $z_i = 1000$ m. For the Gaussian model, $\mathcal{L} = 1.1$ m is assumed.

to be valid only for small integrated values of refractive index fluctuations, i.e., short propagation distances, L , or weak turbulence intensity (Clifford *et al.*, 1974). Measurements (e.g., Daigle *et al.*, 1983) showed a saturation of the variance of the log-amplitude fluctuation with increasing distance. The theory of wave propagation in turbulent media assumes that the wavefront is unperturbed when reaching the eddy responsible for the fluctuation of the refractive index (Daigle *et al.*, 1983). However, for longer paths, the wavefront has been already randomly distorted and, thus, the variation of the refractive index is less effective in producing the log-amplitude fluctuations. Wenzel (1975) formulated a model for the prediction of the saturation distance which showed a rough agreement with measurements (Bertagnolio *et al.*, 2020; Daigle *et al.*, 1983). We found discrepancies in existing literature regarding the saturated value for the variance, $\sigma_{\zeta, \text{sat}}^2$. For example, Daigle *et al.* (1983) reports a maximum value of the saturated standard deviation of no more than 6 dB, corresponding to $\sigma_{\zeta, \text{sat}}^2 \approx 0.48$. This value agrees quite well with the theoretical result $\pi^2/24$, obtained for optics (Hill and Clifford, 1981), but it is rather far from the value (approximately 0.8) found by the recent measurements made by Bertagnolio *et al.* (2020).

A theoretical model for the saturation of the optical scintillations has been developed by Clifford *et al.* (1974) and subsequently improved by Hill and Clifford (1981), but to the best of the authors' knowledge, it has never been applied in acoustics. The analysis of Hill and Clifford (1981) suggests that the saturation phenomenon can be included in the calculation of the correlation function for the log-amplitude fluctuations, i.e., Eq. (7) with the “-” sign, multiplying the integrand by the additional function,

$$M_{\text{ST}} = \exp \left(-48k^2L \left\{ \kappa \Psi[(1 - \eta)h_s + \eta h_r, \kappa] \times [1 - J_0(\kappa^2 U)] + \int_{\kappa}^{\infty} d\kappa' \Psi(z, \kappa') \times [1 - J_0(\kappa' \kappa U)] \right\} \right), \quad (11)$$

where $U = L\eta(1 - \eta)/k$ and $\Psi(z, \kappa) = \int_{\kappa}^{\infty} \Phi_{\text{eff}}(z, \kappa') d\kappa'$. Even if an analytical formula can be obtained for $\Psi(z, \kappa)$ with the von Kármán spectrum, the integral in Eq. (11) does not have a closed-form solution. The computational cost for a numerical evaluation of M_{ST} coupled with the solution of the integral of Eq. (7) is too high for the current implementation. For these reasons, the model of Hill and Clifford (1981) for the saturation of the log-amplitude fluctuations is not applied in this work.

However, it is necessary to limit the value of the correlation function to avoid nonphysical log-amplitude fluctuations. We suggest limiting the value of the variance to $\sigma_{\zeta, \text{sat}}^2 = 0.8$, following the experimental results of Bertagnolio *et al.* (2020). It should be noted that more measurements are necessary to confirm this value and obtain a more precise estimate. In practice, if a value higher than $\sigma_{\zeta, \text{sat}}^2$ is computed using Eq. (7) for $\zeta = 0$, the correlation

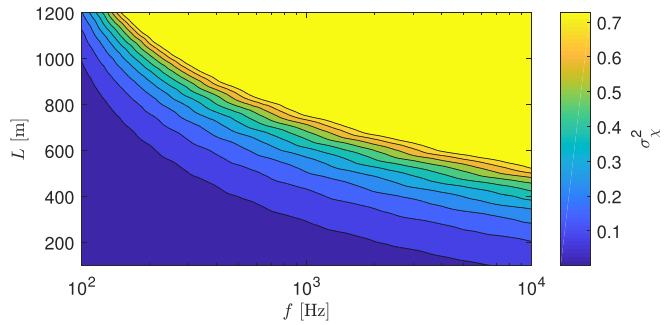


FIG. 4. (Color online) Log-amplitude variance calculated for $h_s = 109$ m and $h_r = 1.5$ m. The atmospheric surface layer is modeled using similarity theories with $Q_H = 50$ W/m², $u_* = 0.3$ m/s, and $z_i = 1000$ m.

function is rescaled, i.e., $B_{\zeta, \text{sat}}(L, \zeta) = B_{\zeta}(L, \zeta) \sigma_{\zeta, \text{sat}}^2 / B_{\zeta}(L, 0)$, to obtain $B_{\zeta, \text{sat}}(L, 0) = \sigma_{\zeta, \text{sat}}^2$. The proposed approach neglects the effects that saturation has on the shape of the correlation function.

Figure 4 shows the log-amplitude variance calculated using Eq. (7) with $\zeta = 0$ and limiting its value to $\sigma_{\zeta, \text{sat}}^2 = 0.8$. The height of the source is set to 109 m to replicate the measurements of Bertagnolio *et al.* (2020). Considering the uncertainties related to the atmospheric conditions, a good agreement can be observed between Fig. 11 of Bertagnolio *et al.* (2020) and Fig. 4 for $u_* = 0.3$ m/s. The values for Q_H and z_i have a small influence on the considered case; hence, reasonable values ($Q_H = 50$ W/m² and $z_i = 1000$ m) are used to generate Fig. 4. As expected, high frequencies saturate at shorter distances, and this behavior is correctly captured by the model proposed.

V. GENERATION OF THE SCINTILLATION SEQUENCE FROM THE CORRELATION FUNCTIONS

A. Theory

A methodology to generate scintillation sequences has been first described by Jurado-Navas *et al.* (2011) and applied to optical scintillations. The same method can also be used in acoustics as described by Rietdijk *et al.* (2017). In the present work, we follow the method described in these references with the difference that two distinct time domain sequences are generated for the phase and log-amplitude fluctuations. The reason is that the correlation functions for the phase and log-amplitude introduced in Sec. III are distinct, whereas for the model explained in Sec. II and used by Rietdijk *et al.* (2017), the correlation functions were identical [Eq. (3)]. Furthermore, a consistent methodology is suggested for the calculation of the velocity used to convert the correlation functions from the space to the time domain.

First, both correlation functions for the phase and log-amplitude fluctuations are evaluated using the methodology described in Sec. III. To reduce the computational cost, the functions are evaluated for 40 points with a cubic distribution¹ between 0 and ζ_{max} and interpolated with cubic splines on $N = 2^{15}$ equally spaced points. ζ_{max} must be large enough to capture the largest turbulence scales. From the

considerations made in Sec. III, $\zeta_{\max,\chi} = 2\sqrt{\lambda L}$ is used for the log-amplitude correlation function because $B_\chi(\zeta_{\max,\chi}) \approx 0$. However, as depicted in Fig. 3, the phase fluctuations are induced by turbulent structures larger than those for the log-amplitude fluctuations. For this reason, a different maximum value is chosen for the evaluation of the phase correlation,

$$\zeta_{\max,\phi} = 20\sqrt{\lambda L}h_{\max}f_{\max}/(h_0f_0), \tag{12}$$

where $h_{\max} = \max(h_s, h_r/3)$, $h_0 = 1$ m, and $f_{\max} = \max(f_0, f)$, $f_0 = 1000$ Hz, has been verified to give $B_\phi(\zeta_{\max,\phi}) \approx 0$ for different propagation distances, frequencies, and source and receiver heights. The correlation functions are finally mirrored around $\zeta = 0$.

Second, Taylor’s hypothesis of frozen turbulence is exploited to convert the correlation functions from the space domain, ζ , to the time domain, τ , using the wind velocity perpendicular to the propagation path, v_\perp (Brown and Hall, 1978; Lawrence and Strohbehn, 1970). The horizontal wind velocity is modeled with the Monin–Obukhov similarity theory as (Ostashev and Wilson, 2016)

$$v(z) = \frac{u_*}{\kappa_v} \left(\ln \left(\frac{z}{z_0} \right) - \psi_m \left(\frac{z}{L_o} \right) + \psi_m \left(\frac{z_0}{L_o} \right) \right), \tag{13}$$

where z_0 is the surface roughness length, and

$$\psi_m(\xi) = \begin{cases} 2 \ln \left[\left(1 + \sqrt{1 + a_m |\xi|^{2/3}} \right) / 2 \right], & \xi < 0 \\ 1 + b_m \xi, & \xi \geq 0, \end{cases} \tag{14}$$

where $a_m = 3.6$ and $b_m = 5.3$. The perpendicular velocity is calculated from the total (horizontal) velocity, Eqs. (13) and (14), and the source-receiver direction and, finally, averaged along the propagation path. However, Taylor’s hypothesis becomes questionable if the fluctuations in the perpendicular velocity are of the same order of magnitude as the mean, i.e., $\sigma_\perp \sim v_\perp$ (Lawrence and Strohbehn, 1970) or, in other terms, if the mean perpendicular velocity becomes equal or lower than its corresponding fluctuations, i.e., $v_\perp \leq \sigma_\perp$. Tatarski (1961) (see also Lawrence and Strohbehn, 1970) suggests that in the limit $v_\perp \rightarrow 0$, v_\perp can be replaced by its standard deviation, σ_\perp . In this work, the maximum value between v_\perp and σ_\perp is used (in the following, the symbol v_\perp will be used regardless to indicate the maximum). The standard deviation of the velocity fluctuations is computed as $\sigma_\perp = \sqrt{(\sigma_{v,s}^2 + \sigma_{v,b}^2)/2}$, where $\sigma_{v,s}^2$ and $\sigma_{v,b}^2$ are calculated using Eq. (9). Formally, Taylor’s frozen turbulence hypothesis is applied as $B_{\phi,\chi}(\zeta) = B_{\phi,\chi}(v_\perp \tau) = R_{\phi,\chi}(\tau)$. The sampling frequency of the fluctuations is $f_s = v_\perp / (\Delta x) = v_\perp / (\zeta_{\max}/N)$.

Then, the double-sided power spectral densities, $S_{\phi,\chi}(f)$, are calculated as the Fourier transform of the correlation functions according to Wiener–Khinchin theorem,

$$S_{\phi,\chi}(f) = \int_{-\infty}^{+\infty} R_{\phi,\chi}(\tau) \exp(-i2\pi f \tau) d\tau. \tag{15}$$

Next, a time domain filter is constructed with frequency response, $H_{\phi,\chi}(f)$, defined as

$$H_{\phi,\chi}(f) = |H_{\phi,\chi}(f)| \exp(-i2\pi f \tau_N) = \sqrt{|S_{\phi,\chi}(f)|} \exp(-i2\pi f \tau_N), \tag{16}$$

where a linear phase factor with constant delay, $\tau_N = \zeta_{\max}/v_\perp$, is applied to obtain a causal filter.

The filter impulse response, $h_{\phi,\chi}(t)$, is finally obtained by taking the inverse Fourier transform of the double-sided response,

$$h_{\phi,\chi}(t) = \int_{-\infty}^{+\infty} H_{\phi,\chi}(f) \exp(i2\pi f t) df. \tag{17}$$

Finally, the time sequences are calculated with a convolution of the filter impulse response with a Gaussian signal, $w(t)$, with unit variance, i.e., $\chi(t) = (h_\chi * w)(t)$ and $\phi(t) = (h_\phi * w)(t)$.

B. Results

Figure 5 shows the resulting sequences. The log-amplitude fluctuations are expressed in decibels and calculated as $20 \log_{10} \exp(\chi(t)) = \chi(t) 20 \log_{10}(e)$. In this case, the application of the decibel scale corresponds to a simple multiplication factor, and it helps to interpret the results perceptually. The parameters of the simulations are the same as those for Fig. 3: horizontal propagation at 2 m height for 100 m in a slightly unstable atmospheric boundary layer. The propagation direction is crosswind: in this case, the transverse wind speed is the total horizontal wind speed calculated with Eq. (13) and $z = 2$ m, resulting in $v_\perp \approx 2.13$ m/s. For the propagation distance considered, the variances calculated with the von Kármán model do not exceed the saturation value chosen ($\sigma_{\chi,\text{sat}} = 0.8$). Instead, the Gaussian model predicts a variance for $f = 2000$ Hz, which is slightly higher than the value of saturation and, hence, $\sigma_{\chi,\text{sat}} = 0.8$ is used for that frequency only. Five frequencies between 125 and 2000 Hz are shown.

In Fig. 5, several differences can be observed between the sequences obtained with the Gaussian and von Kármán models. First, the Gaussian model predicts larger log-amplitude fluctuations: for a tone at 2000 Hz, fluctuations up to 20 dB are predicted by the Gaussian model, whereas the log-amplitude fluctuations of the von Kármán model are limited to 6 dB. Even if these values depend on the atmospheric conditions, source and receiver heights, and distance, the log-amplitude fluctuations predicted by the Gaussian model are larger than those predicted by the von Kármán spectrum in every condition. Furthermore, the modulation spectrums for the log-amplitude and phase fluctuations are different: high-frequency fluctuations are observed only in the sequences obtained with the von Kármán model.

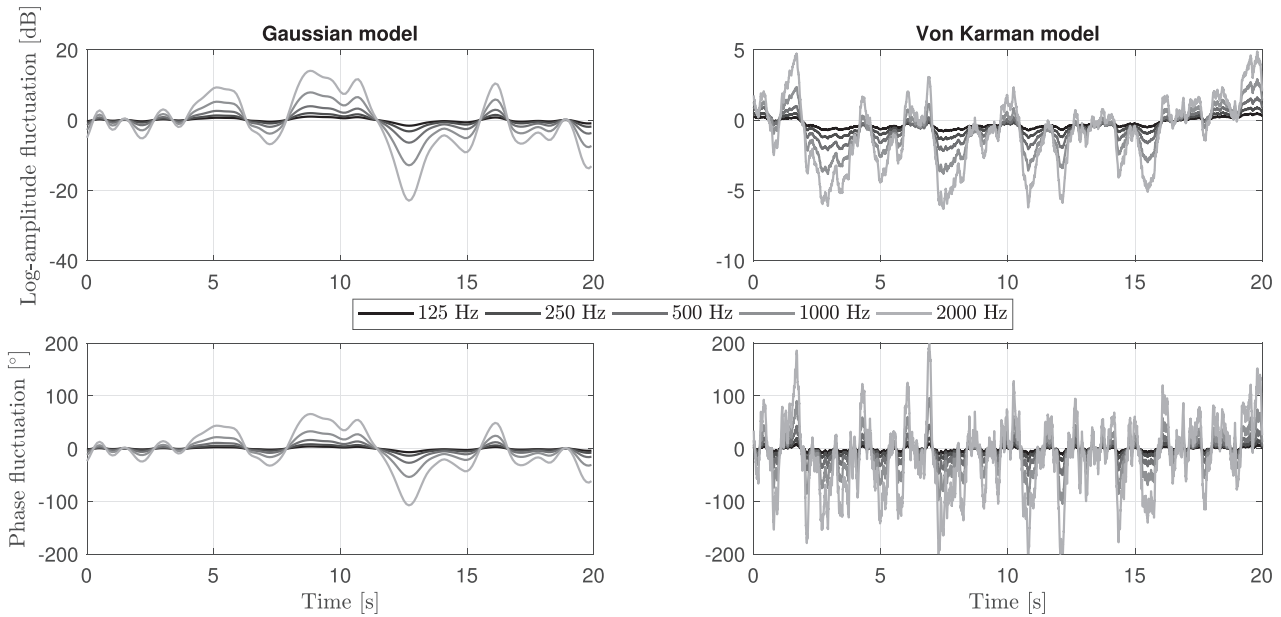


FIG. 5. Log-amplitude (dB) and phase ($^{\circ}$) fluctuations calculated with (left) the Gaussian model and (right) the von Kármán spectrum. The source-receiver distance is $L = 100$ m, and the heights of the source and receiver are $h_s = h_r = 2$ m. The atmospheric surface layer is modeled using similarity theories with $Q_H = 50$ W/m 2 , $u_* = 0.3$ m/s, and $z_i = 1000$ m. For the Gaussian model, it is assumed $\mathcal{L} = 1.1$ m.

This can be explained by the fact that the von Kármán spectrum also models the small turbulent structures responsible for the high-frequency fluctuations, whereas the Gaussian spectrum neglects these structures.

Figures 6–8 show the log-amplitude and phase fluctuations calculated with the von Kármán model for variations of the most relevant parameters and keep the frequency constant at 1000 Hz. Once more, we recall that the assumption of a single, straight propagation path is not strictly verified for all the cases considered. However, the parametric study presented in the last part of this section will help to confirm the expected trends, validate the implementation, and give an estimate of the log-amplitude and phase fluctuations

expected for sound propagating in the atmospheric surface layer.

In Fig. 6, the effect of the propagation direction is exhibited to highlight the effect that the transverse velocity has on the sequences. In particular, it is shown that the fluctuations are slower as the propagation direction goes from crosswind (90°) to downwind (0°). This is a result of the decreasing transverse velocity. For the case of downwind propagation, the transverse velocity is zero and, therefore, the standard deviation of the velocity fluctuations is used instead. As a result, the fluctuations are relatively slower as the transverse velocity decreases. This is valid for log-amplitude and phase fluctuations. To help visualize the

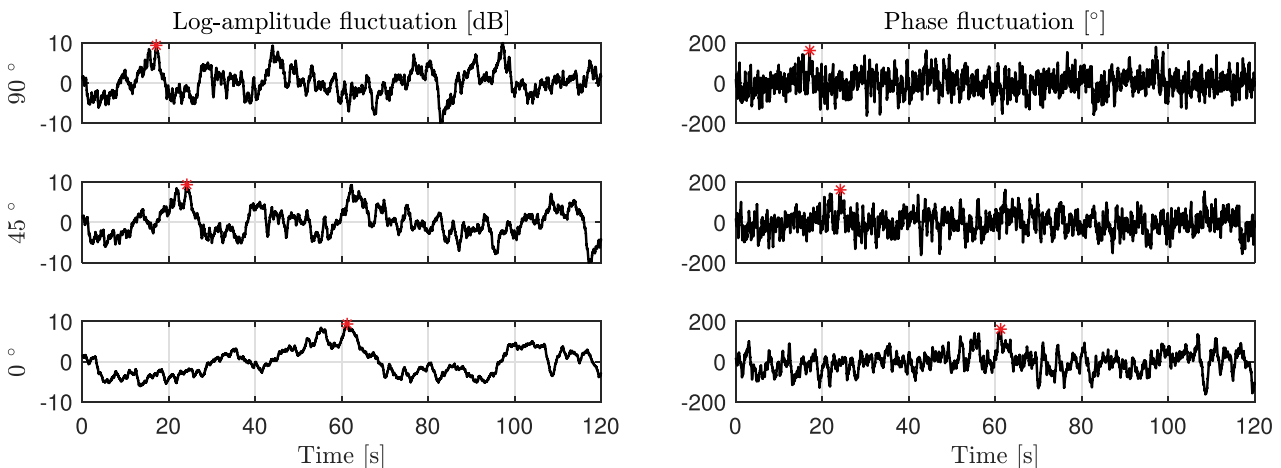


FIG. 6. (Color online) Log-amplitude (dB) (left) and phase ($^{\circ}$) fluctuations (right) calculated with the von Kármán spectrum for different propagation directions: 90° is the crosswind direction, and 0° is downwind. The transverse velocities used are 2.1 and 1.5 m/s for 90° and 45° , respectively. The standard deviation (0.59 m/s) is used instead of the transverse velocity for 0° . The source-receiver distance is $L = 200$ m, the frequency is $f = 1000$ Hz, and the heights of the source and receiver are $h_s = h_r = 2$ m. The atmospheric surface layer is modeled using similarity theories with $Q_H = 50$ W/m 2 , $u_* = 0.3$ m/s, and $z_i = 1000$ m. The red marker traces the same point in the original Gaussian signal, $w(t_0)$.

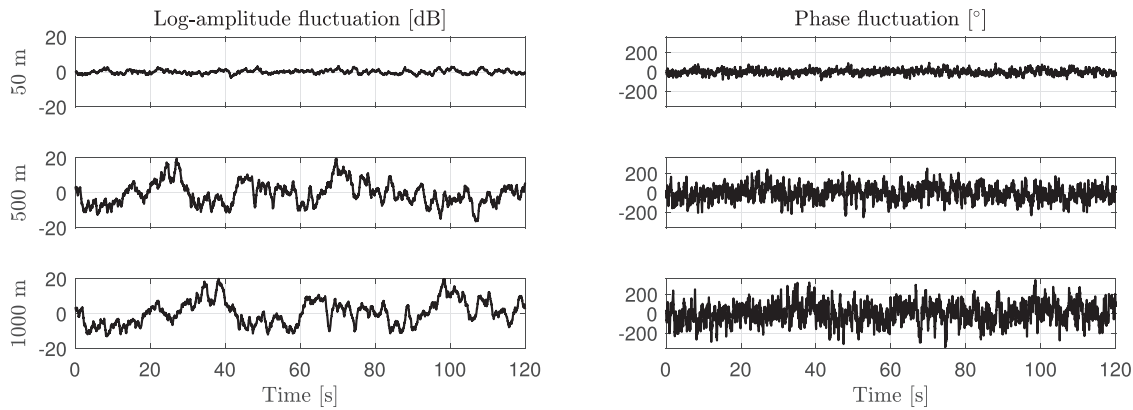


FIG. 7. Log-amplitude (dB) (left) and phase ($^{\circ}$) fluctuations (right) calculated with the von Kármán spectrum for different propagation distances, L , in the crosswind direction. The heights of the source and receiver are $h_s = h_r = 2$ m, and the frequency is $f = 1000$ Hz. The atmospheric surface layer is modeled using similarity theories with $Q_H = 50$ W/m 2 , $u_* = 0.3$ m/s, and $z_i = 1000$ m.

effect of the transverse velocity, a red marker is used in the plots, tracing the same point of the original Gaussian signal, $w(t_0)$, in the resulting sequences, $\chi(t_0)$ and $\phi(t_0)$.

Figure 7 shows the log-amplitude and phase fluctuations for different propagation distances. As expected, the amplitude of the fluctuations increases with increasing distance as the wave is exposed to variations in the refractive index for a longer distance. For the frequency analyzed (1000 Hz), saturation occurs only at approximately 530 m. For this reason, the amplitude of the fluctuations is almost unchanged between the curves at 500 and 1000 m. However, the shape of the correlation function changes with the distance even within the saturated regime: in general, with increasing distance, the contribution from larger eddies is relatively more important and, as a result, fluctuations are slower, i.e., with a lower frequency content. These considerations are valid for log-amplitude and phase fluctuations.

Figure 8 shows the log-amplitude and phase fluctuations for different heights of propagation above the ground. In this case, while fluctuations of the phase increase with the height, the log-amplitude fluctuations decrease. This result is consistent with the theory. As mentioned in Sec. III, the log-amplitude fluctuations are mainly influenced by the

small turbulent structures which characterize the lower part of the atmospheric surface layer. The maximum size of the turbulent eddies increases with the height above ground, thus, the log-amplitude fluctuations are less pronounced for higher sources and receivers. The opposite can be said for the phase fluctuations that are, instead, mostly influenced by the large turbulent structures typical of the upper part of the atmospheric surface layer. The same trends highlighted for Fig. 8 also have been observed with changing source height (not shown), keeping the receiver height and source-receiver distance fixed. Small differences are observed inverting the source and receiver positions (not shown), and they are caused by the Bessel function in Eq. (7), which is not symmetrical. The Bessel function is giving a relatively higher weight to turbulence characteristics close to the source ($\eta = 0$) than close to the receiver ($\eta = 1$). This physical phenomenon is related to the spherical nature of the sound waves and, indeed, the source-receiver reciprocity is retrieved for the plane wave approximation [see Eqs. (7.81) and (7.82) from Ostashev and Wilson, 2016]. We can conclude that the characteristics of the turbulence along the entire propagation path affect the log-amplitude and phase fluctuations.

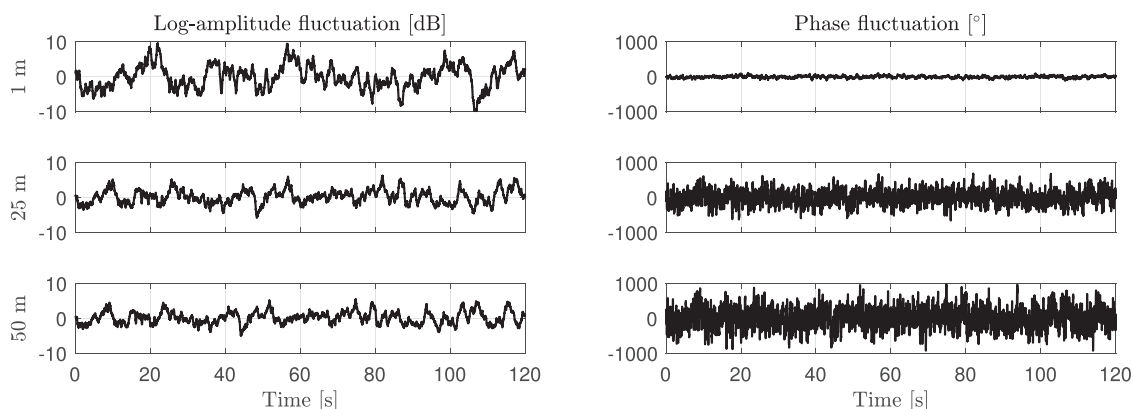


FIG. 8. Log-amplitude (dB) (left) and phase ($^{\circ}$) fluctuations (right) calculated with the von Kármán spectrum for different propagation heights, $h = h_s = h_r$. The source-receiver distance is $L = 200$ m in the crosswind direction, and the frequency is $f = 1000$ Hz. The atmospheric surface layer is modeled using similarity theories with $Q_H = 50$ W/m 2 , $u_* = 0.3$ m/s, and $z_i = 1000$ m.

Finally, observing graphs (not shown) similar to Figs. 6–8, it has been noted that Q_H has a limited influence on the log-amplitude and phase fluctuations. However, only positive values of Q_H between 1 and 300 W/m² were analyzed to satisfy the assumption of the Monin–Obukhov theory, which is limited to unstable conditions. In the range of Q_H analyzed, the amplitude of the fluctuation sequences increased by approximately 50%. Instead, the friction velocity, which is proportional to the wind speed, considerably affects the log-amplitude and phase fluctuations. First, the fluctuations are of larger amplitude, suggesting that they are mainly driven by shear-induced velocity fluctuations. Second, as the transverse velocity is also affected by the friction velocity, the fluctuations are faster with increasing u_* . Even small but fast phase fluctuations can have a considerable effect on the auralized signal because of the periodic nature of the phase.

VI. APPLICATION TO TONAL NOISE AND BAND-FILTERED WHITE NOISE

We propose the auralization of a tonal source in a turbulent atmosphere as the first application of the methodology presented in this paper. We consider the acoustic signal at the receiver position in the absence of turbulence, $y(t) = \sin(2\pi f_t t)$, where f_t denotes the frequency of the tone. In a turbulent atmosphere, this signal will be received at the observer position as $y(t) = \chi(t) \sin(2\pi f_t t + \phi(t))$, i.e., the amplitude and phase of the acoustic signal will vary in time for a turbulent atmosphere. The phase fluctuation, $\phi(t)$, is low-pass filtered with an eighth-order Butterworth filter with cutoff frequency 100 Hz to smooth the fluctuations and remove audible artifacts. The choice of the 100 Hz cutoff frequency was made through informal listening tests. The original and low-pass filtered phase fluctuations for $f_t = 800$ Hz are depicted in Fig. 9. The source and receiver positions and atmospheric conditions in this simulation are the same as those used to produce the results of Fig. 5. The filtering does not modify the considerations made analyzing Figs. 5 and 6 in Sec. V because, as shown in Fig. 9, the filtered and original sequences are almost overlapped when the time scale used in the horizontal axis is on the order of tens of seconds. A zoom for $t < 50$ ms shows the effect of the filtering.

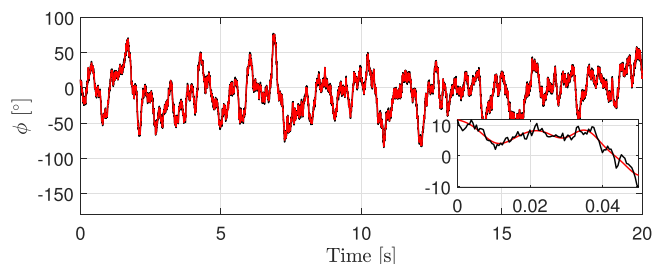


FIG. 9. (Color online) Non-filtered (black line) and low-pass filtered (red line) phase fluctuations for a source signal at 800 Hz. The smaller graph shows a zoom section for the first 50 ms.

Mm. 1–Mm. 4 are audio files obtained for a source height of 80 m, receiver height of 2 m, and distance of 100 m. The atmospheric conditions are representative of a sunny day ($Q_H = 200$ W/m²) and moderate wind speed ($u_* = 0.2$ m/s). The calculated sampling frequency is $f_s \approx 5.1$ kHz. The signals, encoded on 16-bit audio files, have been rescaled with a constant normalization factor such that the overall peak amplitude is half (–6 dBFS) of the full-scale range. A 500 ms fade-in and fade-out windows have also been applied to avoid audible artifacts.

- Mm. 1. 800 Hz pure tone.
- Mm. 2. Phase modulated tone.
- Mm. 3. Amplitude modulated tone.
- Mm. 4. Amplitude and phase modulated tone.

The authors performed informal listening tests to verify the absence of audible artifacts in the audio signals, varying the atmospheric conditions and the source and receiver positions. No artifacts have been detected in the signals with amplitude fluctuations for all conditions tested, suggesting that the proposed methodology is promising for the cases in which amplitude modulation due to turbulence is expected. Signals with low-frequency phase fluctuations, such as those in Mm. 2, are also considered acceptable. However, for vertical and nearly vertical paths, the high-frequency content in the phase fluctuations given by the model produces audio signals with an additional broadband component that is not considered to be physical. This could suggest that the physical model overestimates the high-frequency content of the phase fluctuations. A possible explanation has already been mentioned in Sec. III and it is related to the non-Markov behavior of the phase fluctuation in the atmospheric surface layer. This overestimation is particularly audible for tonal noise. The authors speculate that a more accurate model for the correlation function of the phase fluctuations, e.g., without relying on the Markov approximation (Ostashev *et al.*, 2022; Ostashev and Wilson, 2019), could improve the quality of tonal sounds for the high-frequency phase fluctuations. With such a model, the low-pass filtering of the phase fluctuations might not be necessary. Nevertheless, the model presented here can be implemented as is in several scenarios to improve the realism of auralized broadband noises such as the aerodynamic noise of aircraft flyovers and wind turbines. Indeed, if the single path assumption is verified, the phase fluctuations are not audible due to the random nature of the phase of the aerodynamic sound, whereas amplitude fluctuations are more important and clearly audible.

To demonstrate the applicability of the method described in this work to broadband noise auralization, we present audio files for the same atmospheric conditions and source–receiver configuration previously used for tonal noise (see Mm. 5–Mm. 8). In this case, the sound signal in the absence of turbulence is a band-limited white noise between

561 and 1782 Hz corresponding, respectively, to the lower limit of the 630 Hz 1/3-octave band and upper limit of the 1600 Hz band. The sampling frequency is 44.1 kHz.

The amplitude and phase modulation are frequency dependent and, in principle, the fluctuations should be computed for every frequency. To reduce the computational cost without affecting accuracy, we apply the fluctuations to each 1/3-octave band separately. First, the white noise is filtered into 1/3-octave bands using zero-phase bandpass filters. The filters are 12th-order Butterworth filters. Second, the log-amplitude and phase fluctuations are calculated for the 1/3-octave center frequencies, f_c , and interpolated to obtain the same sampling frequency of the white noise signal (44.1 kHz). The log-amplitude is linearly interpolated, whereas the phase fluctuations are interpolated with third-order polynomials to ensure that the second derivative of the phase fluctuations is continuous, as suggested by Maillard (2009). Then, the fluctuations are applied to each 1/3-octave band separately as

$$y_i(t) = \chi_i(t)W_i\left(t - \frac{\phi_i(t)}{2\pi f_{c,i}}\right), \tag{18}$$

where the subscript “ i ” represents the index of the 1/3-octave band, and $W_i(t)$ is the white noise in the 1/3-octave band, i , in the absence of turbulence. To calculate $W_i(t - \phi_i(t)/2\pi f_{c,i})$, a third-order Lagrange interpolator has been used to obtain high accuracy at high frequency (Laakso *et al.*, 1996). Finally, the signals are recovered by summing the contribution from all the frequency bands. The same Gaussian signal, w , is used for all the frequency bands because the fluctuations are highly correlated between 1/3-octave bands (Pieren *et al.*, 2014). The resulting audio files are given below.

- Mm. 5. Band-limited white noise.
- Mm. 6. Phase modulated white noise.
- Mm. 7. Amplitude modulated white noise.
- Mm. 8. Amplitude and phase modulated white noise.

As expected, the phase modulation does not have any influence on the auralized sound. It is recalled, however, that ground reflection is not considered as a separate contribution. By doing so, the phase fluctuations applied to the interfering direct and ground-reflected waves would probably affect the perceived sound. The maximum modulation in amplitude is between 2 and 4 dB, depending on the frequency, and it can be perceived in Mm. 7 and Mm. 8.

VII. CONCLUSIONS

This paper presents an approach to calculating physics-based acoustic scintillations based on existing theoretical formulations (Kamrath *et al.*, 2021; Ostashev and Wilson,

2018). The correlation functions for the phase and log-amplitude fluctuations are numerically calculated using the von Kármán effective turbulence spectrum for the refractive index fluctuations. The height-dependent variances and length scales for the velocity and temperature fluctuations are computed using the mixed-layer and Monin–Obukhov similarity theories. This approach is compared to the methodology used in previous literature (Heutschi *et al.*, 2014; Rietdijk *et al.*, 2017) based on the Gaussian turbulence spectrum. The model proposed can synthesize more realistic acoustic log-amplitude and phase fluctuations as it is based on theories and results that more accurately capture the real phenomena. The advantage of the approach used in this paper is that it is not necessary to select the turbulence properties at an arbitrary height for slanted propagation: the dependency on the height is inherently considered by the calculation of the correlation functions. Furthermore, the log-amplitude variance calculated with the spherical wave approximation and von Kármán spectrum is closer to the measurements (Kamrath *et al.*, 2021) than the theory based on the Gaussian spectrum (Daigle *et al.*, 1983). A simple empirical model is suggested to take into account the effect of the saturation of the log-amplitude fluctuations for large propagation distances. Finally, the methodology for the calculation of the time sequences from the correlation functions is outlined.

The sequences obtained with the Gaussian spectrum and von Kármán spectrum differ significantly in the frequency content and amplitude of the fluctuations: it is found that the Gaussian spectrum overpredicts the maximum amplitude of the log-amplitude fluctuations by several decibels while it underpredicts the maximum amplitude of the phase fluctuations. As expected, a higher frequency content is observed in the sequences calculated with the von Kármán spectrum.

A sensitivity analysis of the time sequences varying the atmospheric conditions and source-receiver position is presented to confirm the expected trends and quantify the influence of each input parameter. For example, the amplitude of the fluctuations not only increases with increasing propagation distance, but the fluctuations are also slower because the contribution from the larger eddies becomes relatively more important. The propagation distance and friction velocity are the parameters that have the largest influence on the log-amplitude fluctuations. In addition to distance and friction velocity, the phase fluctuations are also strongly affected by the propagation height.

Finally, the audio files for two applications are presented: a simple tone and band-limited white noise propagating in a turbulent atmosphere. In the case of tonal noise, the amplitude and phase fluctuations were audible, and no artifacts were detected by informal listening tests performed by the authors. However, for atmospheric conditions that would produce high-frequency phase fluctuations, the resulting sounds are not considered satisfactory. For this reason, possible solutions that could be developed in future works are suggested. The case of band-limited white noise is

interesting as it is representative of the broadband aerodynamic noise generated, e.g., by aircraft and wind turbines. In this case, the phase fluctuations are not audible due to the randomness of the phase of the white noise and because the ground-reflected wave is not considered as a separate contribution. Instead, the turbulence-induced amplitude modulation is perceivable, and the resulting audio signals do not present audible artifacts.

Future works will analyze the effect of turbulence-induced amplitude modulation on the auralized broadband aerodynamic noise emitted by a wind turbine.

ACKNOWLEDGMENTS

The European Commission supported this research through the H2020-MSCA-ITN-209 project zEPHYR (Grant Agreement No. 860101).

¹Each point ζ_i of a stencil with a cubic distribution is given by $\zeta_i = (i\Delta\zeta)^3 / \zeta_{\max}^2$ for i between 0 and $N - 1$, where N is the number of points and $\Delta\zeta = \zeta_{\max} / (N - 1)$.

Arntzen, M., and Simons, D. G. (2014). "Modeling and synthesis of aircraft flyover noise," *Appl. Acoust.* **84**, 99–106.

Bertagnolio, F., Fischer, A., Shen, W., Vignaroli, A., Hansen, K., Hansen, P., and Søndergaard, L. (2020). "Analysis of noise emission from a single wind turbine at large distances," in *Forum Acusticum 2020*, Lyon, France, 20–24 April 2020, available at <https://hal.science/FA2020/hal-03233754v1> (Last viewed 15 August 2023).

Biesheuvel, J., Tuinstra, M., de Santana, L. D., and Venner, K. (2019). "Effect of turbulent boundary layer induced coherence loss on beamforming measurements in industrial scale wind tunnel tests," in *25th AIAA/CEAS Aeroacoustics Conference*, Delft, The Netherlands, 20–23 May 2019 (AIAA, Reston, VA), available at <https://arc.aiaa.org/doi/abs/10.2514/6.2019-2463> (Last viewed 15 August 2023).

Brown, E. H., and Hall, F. F., Jr. (1978). "Advances in atmospheric acoustics," *Rev. Geophys.* **16**(1), 47–110, <https://doi.org/10.1029/RG016i001p00047>.

Clifford, S. F., Ochs, G. R., and Lawrence, R. S. (1974). "Saturation of optical scintillation by strong turbulence," *J. Opt. Soc. Am.* **64**(2), 148–154.

Daigle, G. A., Piercy, J. E., and Embleton, T. F. W. (1978). "Effects of atmospheric turbulence on the interference of sound waves near a hard boundary," *J. Acoust. Soc. Am.* **64**(2), 622–630.

Daigle, G. A., Piercy, J. E., and Embleton, T. F. W. (1983). "Line-of-sight propagation through atmospheric turbulence near the ground," *J. Acoust. Soc. Am.* **74**(5), 1505–1513.

Heutschi, K., Pieren, R., Müller, M., Manyoky, M., Wissen Hayek, U., and Eggenschwiler, K. (2014). "Auralization of wind turbine noise:

Propagation filtering and vegetation noise synthesis," *Acta Acust. Acust.* **100**(1), 13–24.

Hill, R. J., and Clifford, S. F. (1981). "Theory of saturation of optical scintillation by strong turbulence for arbitrary refractive-index spectra," *J. Opt. Soc. Am.* **71**(6), 675–686.

Jurado-Navas, A., Garrido-Balsells, J. M., Castillo-Vázquez, M., and Puerta-Notario, A. (2011). "A computationally efficient numerical simulation for generating atmospheric optical scintillations," in *Numerical Simulations of Physical and Engineering Processes*, edited by J. Awrejcewicz (IntechOpen, Rijeka), Chap. 7.

Kamrath, M. J., Ostashev, V. E., Wilson, D. K., White, M. J., Hart, C. R., and Finn, A. (2021). "Vertical and slanted sound propagation in the near-ground atmosphere: Amplitude and phase fluctuations," *J. Acoust. Soc. Am.* **149**(3), 2055–2071.

Laakso, T., Valimäki, V., Karjalainen, M., and Laine, U. (1996). "Splitting the unit delay [fir/all pass filters design]," *IEEE Signal Process. Mag.* **13**(1), 30–60.

Lawrence, R., and Strohbehn, J. (1970). "A survey of clear-air propagation effects relevant to optical communications," *Proc. IEEE* **58**(10), 1523–1545.

Lincke, D., Schumacher, T., and Pieren, R. (2023). "Synthesizing coherence loss by atmospheric turbulence in virtual microphone array signals," *J. Acoust. Soc. Am.* **153**(1), 456–466.

Maillard, J. (2009). "Prediction and auralization of construction site noise," in *Proceedings of EURONOISE*, 26–28 October, Edinburgh, Scotland (Institute of Acoustics, Milton Keynes, UK).

Ostashev, V., and Wilson, D. (2016). *Acoustics in Moving Inhomogeneous Media* (Taylor and Francis, London).

Ostashev, V., and Wilson, D. (2018). "Statistical characterization of sound propagation over vertical and slanted paths in a turbulent atmosphere," *Acta Acust. Acust.* **104**, 571–585.

Ostashev, V. E., Shabalina, E., Wilson, D. K., and Kamrath, M. J. (2022). "Non-Markov behavior of acoustic phase variance in the atmospheric boundary layer," *Waves Random Complex Media* (published online).

Ostashev, V. E., and Wilson, D. K. (2019). "Non-Markov character of the phase fluctuations for sound propagation over relatively small ranges in the turbulent atmosphere," *J. Acoust. Soc. Am.* **145**(6), 3359–3369.

Pieren, R., Heutschi, K., Müller, M., Manyoky, M., and Eggenschwiler, K. (2014). "Auralization of wind turbine noise: Emission synthesis," *Acta Acust. Acust.* **100**(1), 25–33.

Pieren, R., and Lincke, D. (2022). "Auralization of aircraft flyovers with turbulence-induced coherence loss in ground effect," *J. Acoust. Soc. Am.* **151**(4), 2453–2460.

Rietdijk, F., Forssén, J., and Heutschi, K. (2017). "Generating sequences of acoustic scintillations," *Acta Acust. Acust.* **103**, 331–338.

Rizzi, S. A., and Sahai, A. K. (2019). "Auralization of air vehicle noise for community noise assessment," *CEAS Aeronaut. J.* **10**, 313–334.

Tatarski, V. I. (1961). *Wave Propagation in a Turbulent Medium* (McGraw-Hill, New York), translated by R. S. Silverman.

Wenzel, A. (1975). "Saturation effects associated with sound propagation in a turbulent medium," in *Progress in Astronautics and Aeronautics*, Hampton, VA, 24–26 March 1975 (AIAA, Reston, VA), pp. 67–75.